UK Atomic Energy Authority

UKAEA-STEP-PR(23)07

R. T. Osawa, D. Moulton, S. L. Newton, S. Henderson, B. Lipschultz, A. Hudoba

SOLPS-ITER analysis of a proposed STEP double null geometry: impact of the degree of disconnection on power-sharing

SOLPS-ITER analysis of a proposed STEP double null geometry: impact of the degree of disconnection on power-sharing

R. T. Osawa, D. Moulton, S. L. Newton, S. Henderson, B. Lipschultz, A. Hudoba

This is a preprint of a paper submitted for publication in Nuclear Fusion

SOLPS-ITER analysis of a proposed STEP double null geometry: impact of the degree of disconnection on power-sharing

R. T. Osawa[1*], D. Moulton[1], S. L. Newton[1], S. Henderson[1], B. Lipschultz[2], A. Hudoba[1]

[1]UKAEA-CCFE, Culham Science Centre, Abingdon, OX14 3DB, United Kingdom
[2]Department of Physics, University of York, Heslington, York, YO10 5DD, United Kingdom
E-mail: ryoko.osawa@ukaea.uk

Aug 2022

Abstract. To mitigate the issue of plasma exhaust in reactor scale tight aspect ratio tokamaks such as STEP (Spherical Tokamak for Energy Production), a double-null (DN) configuration is thought to be advantageous over a single-null (SN) configuration. However, practical control of the plasma vertical stability will likely lead to an oscillation around the symmetry point, which may lead to transient loading of the divertors. In this work we investigated the impact of disconnection of the two separatrices δR_{sep} on the power-sharing between the divertors in disconnected-double-null (DDN) configurations for an early STEP design using the SOLPS-ITER code without drifts. The power fraction to the primary divertor increased with δR_{sep}, reaching $\sim 95\%$ at the highest δR_{sep} which is representative of SN. The total power fraction to the inner divertors (upper + lower), however, did not show an increase with δR_{sep} for $\delta R_{\mathrm{sep}}/\lambda_q \leq 2$, where λ_q is the parallel heat flux decay length, and even at the highest δR_{sep} it showed only $\sim 30\%$ increase from connected-double-null (CDN), unlike the experimental results on current conventional aspect ratio machines. We found two underlying mechanisms that could explain this result - the total flux compression from the outer midplane to the primary inner divertor target and the parallel current in the primary SOL (between the two separatrices). This work implies that the benefit of DN over SN in power load onto the inner divertor in STEP may be less than found experimentally in conventional tokamak due to its tight aspect ratio. Further investigations by experiments especially on STs and simulations with additional physics such as drifts are the subject of a future investigation.

1 Introduction

Plasma exhaust is a key challenge for the STEP (Spherical Tokamak for Energy Production) programme. As STEP aims at producing net energy from a prototype fusion energy plant, the power crossing the separatrix in STEP can be much larger than that handled in existing experimental devices. In a single-null (SN) configuration, combined with the low aspect ratio of a spherical tokamak ($R/a \sim 1.6$), the situation

is difficult for the inner divertor target due to the small radius of the strike point and limited space for power mitigation.

To avoid this, we have been assessing a double-null (DN) configuration as a promising solution for STEP, as the majority of the power can flow into the outer targets which can be located at large major radius. This benefit of DN can especially be beneficial for STs where the situation for the inner divertor targets is difficult as described above. However, practical control of the plasma vertical stability will likely lead to an oscillation around the perfect symmetry point, where both X-points exist on the last closed flux surface. This leads to a disconnected double-null (DDN) configuration that has a gap between the two separatrices.

This gap, usually quantified by the distance between the two separatrices at the outer-midplane δR_{sep}, could be a critical matter for the primary inner target in DDN. In a connected double-null configuration (CDN), power from the outer-midplane (omp) flows towards the two outer divertors. In DDN, on the other hand, the inner and outer targets are now linked by magnetic field lines, i.e. the power from the omp can partly flow to the primary inner divertor. Furthermore, if δR_{sep} reaches values similar to the radial exponential decay length of the SOL at the midplane, it would lead to near single-null loads onto the primary inner divertor target. The increase of the inflow power can be critical for the inner target in a ST due to the small radius of the strike point and limited space.

To assess the impact of disconnection, several experimental studies and a few numerical/theoretical studies have been carried out so far. As a numerical study, the B2.5 code[1] was used in DDN geometries of the Tokamak de Varennes (TdeV), which showed pronounced up-down asymmetry on the outer targets even with a relatively small level of disconnection[2]. As for the experimental studies, the power asymmetry was assessed on MAST in L-mode discharges[3], and also in H-mode discharges[4][5]. In [3], different in-out power ratios were found for lower and upper SN discharges - the fraction to the inner was $\sim$ 20 % for the lower SN, whilst $\sim$ 10 % for the upper SN, which implied a contribution of $\nabla \mathbf{B}$ drift which directed downwards for ions in this case. Another important fact here is that the fraction to the inner $\sim$ 20 % is lower than that reported in similar experiments on conventional aspect ratio tokamaks such as DIII-D [6] and Alcator C-Mod[7] where $\sim$ 30 % of the power flows to the inner divertors in SN discharges. In [7], to assess the dependence of the power-sharing on δR_{sep} in a more quantitative way, semi-analytic formulations to describe the dependence of the power-sharing were introduced - we call this set of formulations "Brunner's model" hereafter in this paper. In addition, they suggested a scaling function of parameters in the model for other machines which has dependence on parallel heat flux decay length λ_q and poloidal magnetic field B_p. Using that scaling, the Brunner's model was applied to STEP that has similar λ_q and larger B_p compared to Alcator C-Mod[8]. This work suggested that null balance to better than 1 mm is required for STEP.

The ultimate goal is to clarify the benefits of DN in terms of plasma exhaust compared to SN and understand the underlying mechanisms that dictate the power

balance in DDN. Towards this goal, the research presented here includes our analysis of the impact of δR_{sep} (≥ 0) on the power-sharing in STEP.

This paper is constructed as follows: Section 2 introduces the SOLPS-ITER simulation setup for a δR_{sep} scan we performed in this study. Then in Sec. 3, a description of a part of Brunner's model is given, which is used in this study to better understand the numerical results of the up-down power sharing. The simulation results are given in Sec.4, for the up-down power sharing (Sec. 4.1) and for the in-out power sharing (Sec. 4.2). As for the up-down sharing, the power fraction to the primary divertor (upper divertor in the investigated cases) increased with δR_{sep}, reaching $\sim 95\%$ at the highest δR_{sep} which is representative of SN. As for the in-out power sharing, however, the total power fraction to the inner divertors (upper + lower), did not show an increase with δR_{sep} for $\delta R_{\text{sep}}/\lambda_q \leq 2$, where λ_q is the parallel heat flux decay length at the outer mid-plane, and even at the highest δR_{sep} it showed only $\sim 30\%$ increase from CDN, unlike the experimental results on current machines. To further analyse the in-out power sharing, Sec. 4.2 is divided into three sub-sections, Sec. 4.2.1 for the radial heat transport through the primary separatrix, Sec. 4.2.2 for the power loss in the main SOL, and Sec. 4.2.3 for the parallel heat transport in the primary SOL. Two important effects that reduced the power fraction to the inner divertor in the primary SOL are further discussed separately - the total flux expansion/compression (Sec. 4.2.3.1) and the parallel current (Sec. 4.2.3.2). A detailed discussion for the parallel current is given in Sec. 5 and conclusions are given in Sec. 6.

2 SOLPS-ITER setup

SOLPS-ITER[11][12] is an integrated code, incorporating the multi-species fluid code B2.5 and the kinetic Monte-Carlo neutral code Eirene. We utilised this code to model a proposed design of STEP with upper-primary DDN configurations. Since drifts are not switched on, the analysis is identical when using the upper or lower divertor as the primary divertor. The distance between the two separatrices, δR_{sep}, was scanned stepwise from 0 mm to 4 mm, with the parallel heat flux decay length $\lambda_q \sim 2$ mm across the scan.

The numerical grid for the $\delta R_{\text{sep}} = 2$ mm case is shown in Fig. 1. For around 1.0GW fusion power with Q = fusion power/auxiliary power ≈ 10 and 70% core radiation, one can figure out the power crossing the separatrix is $\sim$ 100MW. The energy flux at the core boundary was therefore set as $P_{\text{in}} = 100$MW, divided equally between ions and electrons. By dividing the fusion power (1.0 GW) by the energy released per reaction (2.8×10^{12} J = 17.6 MeV), we obtain an expected helium production rate $\alpha = 3.5 \times 10^{20}\,\text{s}^{-1}$. Given this number, the ion particle flux through the core boundary Γ_{in} was set $\Gamma_{\text{in}} = 3.5 \times 10^{22}\,\text{s}^{-1}$, based on the simulations on ITER which set this flux consistent with core fuelling and fusion power production[13]. The radial particle transport coefficient $D_\perp$ and the radial heat transport coefficient for the ions and the electrons $\chi_\perp$ were set to be $D_\perp = 0.3\ \text{m}^2/\text{s}$ and $\chi_\perp = 1.0\ \text{m}^2/\text{s}$, respectively.

The wall geometry and all puff/pump locations were set to be up-down symmetric (Fig. 1(a)). Thus, the inputs to the CDN case ($\delta R_{\mathrm{sep}} = 0$ mm) were perfectly up-down symmetric including the equilibrium. Puffing slots of deuterium molecules were placed in the top/bottom Private Flux region (PFR) near the X-points. To get the target loads down to manageable level, argon gas was seeded from the PFR-side corner of the outer targets, as shown in Fig. 1(b). In B2.5, all the charge states of argon were individually solved as well as the deuterium ion. The pumping ducts were set in the outer legs (two ducts in total) and the pumping speed was set as 131 m^3/s for each duct, independently of pumped species. The tungsten wall temperature of the duct and the pumping tube was set to 306.85 °C (0.04998 eV), while it was set to 857.85 °C (0.09749 eV) for the rest of the wall, expecting it to run warm. The sputtering of the wall was not modelled in the simulations.

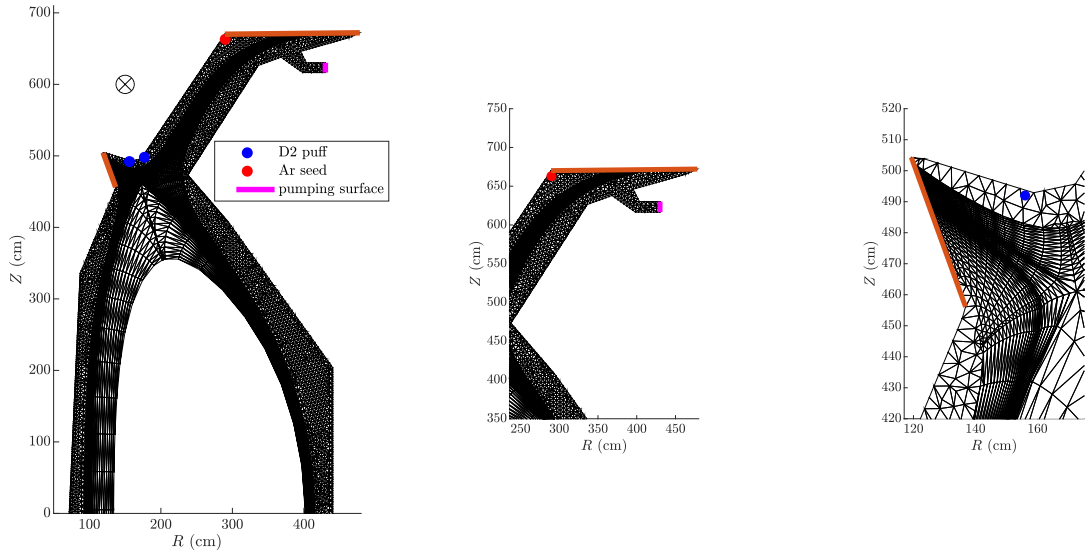

Figure 1: The grid, fueling and pumping locations in SOLPS-ITER for $\delta R_{\mathrm{sep}} = 2$ mm cases.

All drift terms were deactivated in this study. Effects due to the drifts will be assessed and reported elsewhere in the future. While the drifts were deactivated, the currents (parallel currents and a small anomalous radial current) were activated in the plasma solver.

3 Brunner's model

Brunner's model[7] was formulated to estimate power-sharing between the 4 divertors in DDN (Fig. 2 (a)). It consists of two parts, 1) in-out sharing and 2) up-down sharing.

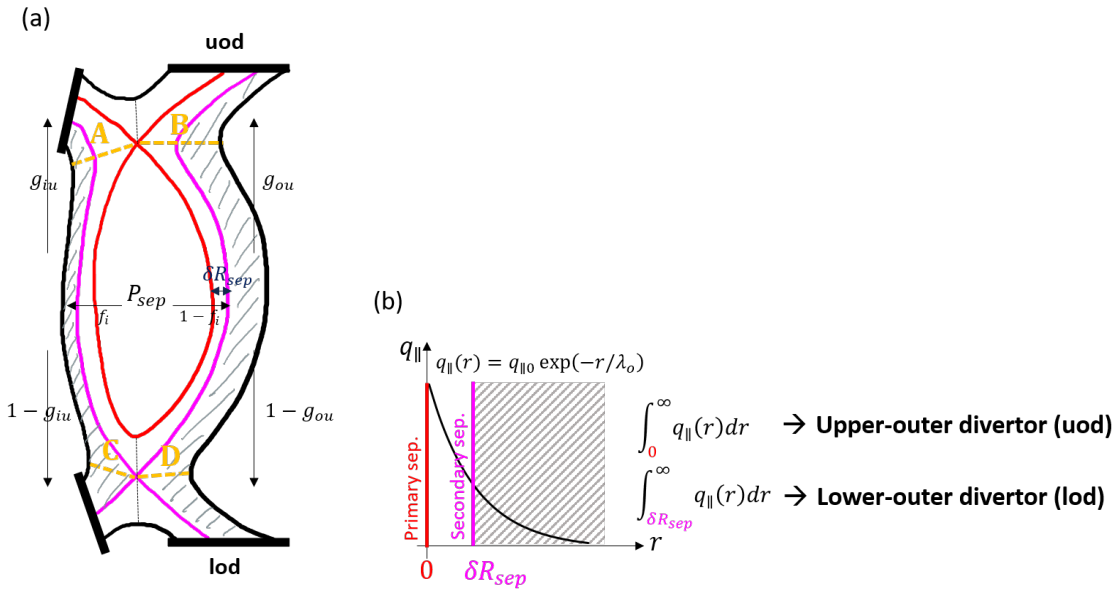

Figure 2: (a) Schematic view of Brunner's model – a model for power-sharing between 4 divertors in DDN. (b) Assumed profile of the parallel heat flux along the outer midplane in the model.

For the power-sharing we consider the power flowing into each divertor, rather than that reaching each divertor target after dissipation. Thus we define the power flowing into each divertor entrance (the surfaces A, B, C, and D in Fig. 2(a)) as $P_{\rm uide}$, $P_{\rm uode}$, $P_{\rm lide}$, and $P_{\rm lode}$, for the upper-inner, upper-outer, lower-inner, and the lower-outer divertor entrances, respectively. The power coming through the separatrix $P_{\rm sep}$ is split between the 4 divertors and the side walls. Assuming that the fraction to the side walls is negligibly small and there is no radiation in the SOL in the steady state we have:

$$P_{\rm sep} \sim P_{\rm dive,tot} = P_{\rm lide} + P_{\rm uide} + P_{\rm uode} + P_{\rm lode}. \tag{1}$$

In-out sharing is defined with $f_{\rm i}$, the power fraction going to the inner divertors, as

$$f_{\rm i} = \frac{(P_{\rm lide} + P_{\rm uide})}{P_{\rm dive,tot}}. \tag{2}$$

The in-out sharing is followed by up-down sharing separately for the outer and inner divertors. For the outer divertors, it is defined by $g_{\rm ou}$, the power fraction going to the upper-outer divertor, such that

$$g_{\rm ou} = \frac{P_{\rm uode}}{(P_{\rm uode} + P_{\rm lode})}. \tag{3}$$

A theoretical expression for $g_{\rm ou}$ can be obtained by the assumptions that 1) the parallel heat flux density decays exponentially with a characteristic length $\lambda_{\rm o}$ at the outer midplane and 2) the power crossing the secondary separatrix is equally divided amongst

the upper and the lower divertors. From the first assumption, we can describe the power going to the upper-outer divertor (from the omp) as

$$P_{\mathrm{uode}} = \int_0^\infty q_{||}(r)dr. \tag{4}$$

From the second assumption, the power going to the lower-outer divertor is equal to that going to the upper-outer via the secondary SOL, thus

$$P_{\mathrm{lode}} = \int_{\delta R_{\mathrm{sep}}}^\infty q_{||}(r)dr. \tag{5}$$

This gives us the theoretical expression of g_{ou},

$$g_{\mathrm{ou}} = \frac{\int_0^\infty q_{\parallel}(r)dr}{\int_0^\infty q_{\parallel}(r)dr + \int_{\delta R_{\mathrm{sep}}}^\infty q_{\parallel}(r)dr} = \frac{\exp\left(\delta R_{\mathrm{sep}}/\lambda_{\mathrm{o}}\right)}{1+\exp\left(\delta R_{\mathrm{sep}}/\lambda_{\mathrm{o}}\right)}. \tag{6}$$

As for the inboard side, one may think that the same model for the outboard side cannot be applied, because a large part of the power to the inner divertors could originate as power from the LFS in addition to the radial power from the HFS. Despite this, Eq. 6 was found reasonable also to describe the up-down power sharing of the inner divertors in the experimental results of [7], as long as a different decay length parameter, λ_{i} instead of λ_{o}, is taken into account. The power fraction to the upper-inner divertor g_{iu} then is described as

$$g_{\mathrm{iu}} = \frac{\exp\left(\delta R_{\mathrm{sep}}/\lambda_{\mathrm{i}}\right)}{1+\exp\left(\delta R_{\mathrm{sep}}/\lambda_{\mathrm{i}}\right)} = \frac{\exp\left(\delta R_{\mathrm{sep,inn}}/\lambda_{\mathrm{i,inn}}\right)}{1+\exp\left(\delta R_{\mathrm{sep,inn}}/\lambda_{\mathrm{i,inn}}\right)}. \tag{7}$$

Here we introduced $\delta R_{\mathrm{sep,inn}}$, the distance between the two separatrices at the inner-midplane (imp), and $\lambda_{\mathrm{i,inn}}$, the corresponding parameter for the inboard up-down power sharing. They can be described as

$$\delta R_{\mathrm{sep,inn}} = \alpha_{\mathrm{pol}}\delta R_{\mathrm{sep}}, \quad \lambda_{\mathrm{i,inn}} = \alpha_{\mathrm{pol}}\lambda_{\mathrm{i}}, \tag{8}$$

where α_{pol} is a poloidal flux expansion from the omp to the imp.

To summarise, the power going to each divertor is given by the model to be:

- Lower-inner: $f_{\mathrm{i}}(1-g_{\mathrm{iu}})$
- Upper-inner: $f_{\mathrm{i}}g_{\mathrm{iu}}$
- Upper-outer: $(1-f_{\mathrm{i}})g_{\mathrm{ou}}$
- Lower-outer: $(1-f_{\mathrm{i}})(1-g_{\mathrm{ou}})$

In this study, we use the second part of Brunner's model, the model for the up-down power-sharing with g_{ou} and g_{iu}. The correspondence between the model definitions and the SOLPS-ITER quantities is shown in Tab. 1.

Table 1: Correspondence between Brunner's model and SOLPS-ITER.

	Description in the model	SOLPS-ITER
g_{ou}	$\frac{\exp(\delta R_{\mathrm{sep}}/\lambda_{\mathrm{o}})}{1+\exp(\delta R_{\mathrm{sep}}/\lambda_{\mathrm{o}})}$	$\frac{P_{\mathrm{uode}}}{(P_{\mathrm{uode}}+P_{\mathrm{lode}})}$
g_{iu}	$\frac{\exp(\delta R_{\mathrm{sep}}/\lambda_{\mathrm{i}})}{1+\exp(\delta R_{\mathrm{sep}}/\lambda_{\mathrm{i}})} = \frac{\exp\left(\delta R_{\mathrm{sep,inn}}/\lambda_{\mathrm{i,inn}}\right)}{1+\exp\left(\delta R_{\mathrm{sep,inn}}/\lambda_{\mathrm{i,inn}}\right)}$	$\frac{P_{\mathrm{uide}}}{(P_{\mathrm{uide}}+P_{\mathrm{lide}})}$

4 SOLPS-ITER modelling results

The cases performed in this study are detailed in Tab.2. In the steady state, the target electron temperature at the strike point ranges from 1 eV to 2 eV for the inner divertors, from 0.5 to ∼20 eV for the outer divertors, which supports that most of the cases are not far from the operational regime. However, the peak temperature at the primary inner target remained high (∼30 eV) in the far SOL in all the cases, because of the feature of vertical targets. The inputs were up-down symmetric, except for the equilibria for the DDN cases ($\delta R_{\mathrm{sep}} > 0$mm).

Figures 3 (a) and (b) show the SOLPS-ITER predictions of power sharing between the 4 divertors as a function of δR_{sep}. To support the color map shown in Fig. 3(a), the ratio to each divertor is shown in Fig. 3(b). The features of the power-sharing were consistent across the cases, thus the result of Case No. 3 is shown here as a representative in both figures.

Table 2: Investigated cases in SOLPS-ITER. The four different colors will be used in some figures hereafter such as Fig.4 to distinguish the cases (Case No. 1-4).

Case No.	D2 puff ($\times 10^{23}$ /s)	Ar puff ($\times 10^{21}$ /s)	δR_{sep} (mm)						
			0	1	2	3	4	7	12
1	2.0	6	-	✓	✓	✓	✓	-	-
2	2.0	8	-	✓	✓	✓	✓	✓	✓
3	3.0	8	✓	✓	✓	✓	✓	✓	✓
4	3.0	10	✓	✓	✓	✓	✓	-	-

To better understand these figure, we will first focus on up-down power sharing, investigating how well the SOLPS-ITER results follow Brunner's model. Brunner's model has a single unknown parameter for the up-down sharing for each side, λ_{o} for the outboard and λ_{i} ($\lambda_{\mathrm{i,inn}}$) for the inboard side, as shown in Eqs. 6 and 7. We quantify the agreement with Brunner's model by fitting the parameters λ_{o} and $\lambda_{\mathrm{i,inn}}$ to the simulation data of up-down sharing, and comparing those fitted values to the actual parallel heat flux decay lengths in the simulation, $\lambda_{\mathrm{q,out}}$ for the outboard and $\lambda_{\mathrm{q,inn}}$ for the inboard.

Secondly we study in-out power sharing. An interesting finding in Fig. 3(a) is that the total power fraction to the inner divertors, f_{i} in Eq. 2 shown by the boundary between the green and the blue colors, does not increase for $\delta R_{\mathrm{sep}} \leq 4$ mm, corresponding to $\delta R_{\mathrm{sep}}/\lambda_{\mathrm{q,out}} \leq 2$, though the power ratio to the upper-inner divertor slightly increases

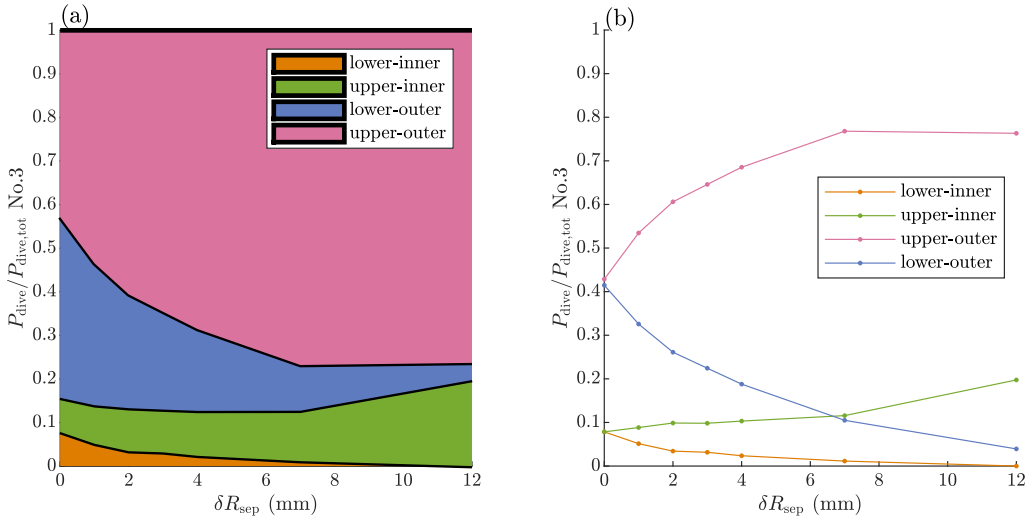

Figure 3: SOLPS-ITER predictions of power sharing between the 4 divertors $P_{\rm dive}/P_{\rm dive,tot}$ as a function of $\delta R_{\rm sep}$ for Case No. 3 in Tab. 2 (Color map). The markers show the total power fraction to the inner divertors f_i, as given in Eq. 2, for all the cases given in Tab. 2. The colors of markers correspond to the case numbers given in the first column of Tab. 2.

as shown in Fig. 3(b), which is unlike the experimental results[3][7]. To understand the physical mechanisms producing this behaviour, two different sources/sinks that are not in the model have been examined: the radial heat flux through the primary separatrix (Sec. 4.2) and the parallel energy transport in the primary SOL which links inboard and outboard sides (Sec. 4.2.3). Only the results of $0 \leq \delta R_{\rm sep}/\lambda_{\rm q,out} \leq 2$ ($0 \leq \delta R_{\rm sep} \leq 4$mm) will be assessed in detail for the in-out sharing.

4.1 UP-DOWN sharing

Power sharing between the upper and lower divertor was investigated separately for the outboard and the inboard side. The total energy flux at each divertor entrance, which was used for calculating the power sharing, is well-represented by the summation of the total conduction $q_{\rm cond}$, total convection $q_{\rm conv}$, and the energy flux carried by the electron thermal current $q_{\rm thermj}$, such that

$$q_{\rm tot} = q_{\rm cond} + q_{\rm conv} + q_{\rm thermj}, \tag{9}$$

where

$$q_{\rm cond} = q_{\rm conde} + q_{\rm condi} = -A_{\parallel}\left(\kappa_{\parallel e} b_x^2 \frac{\partial T_e}{h_x \partial x} + \kappa_{\parallel i} b_x^2 \frac{\partial T_i}{h_x \partial x}\right), \tag{10}$$

$$q_{\rm conv} = q_{\rm conve} + q_{\rm convi} = A_{\parallel} b_x \left(\frac{5}{2} n T_e (V_{\parallel} - j_{\parallel}/en) + \Sigma_a \frac{5}{2} n_a T_i V_{a\parallel}\right), \tag{11}$$

$$q_{\rm thermj} = -A_{\parallel} b_x \left(0.71 j_{\parallel} T_e/e\right). \tag{12}$$

Here $A_\parallel$ is the parallel area, $\kappa_{\parallel e}$ and $\kappa_{\parallel i}$ are the parallel conductivity for the electron and D ion respectively, $b_x = B_x/B$ with B_x the poloidal magnetic field, x is the poloidal coordinate, h_x is the metric coefficient for the poloidal coordinate, and T_e,T_i,n,$V_\parallel$,n_a,$V_{a\parallel}$,$j_\parallel$, and e are the electron and ion temperature, electron density, D^+ parallel flow velocity, density for ion species a, parallel velocity for ion species a, the parallel current, and the unit of charge, respectively.

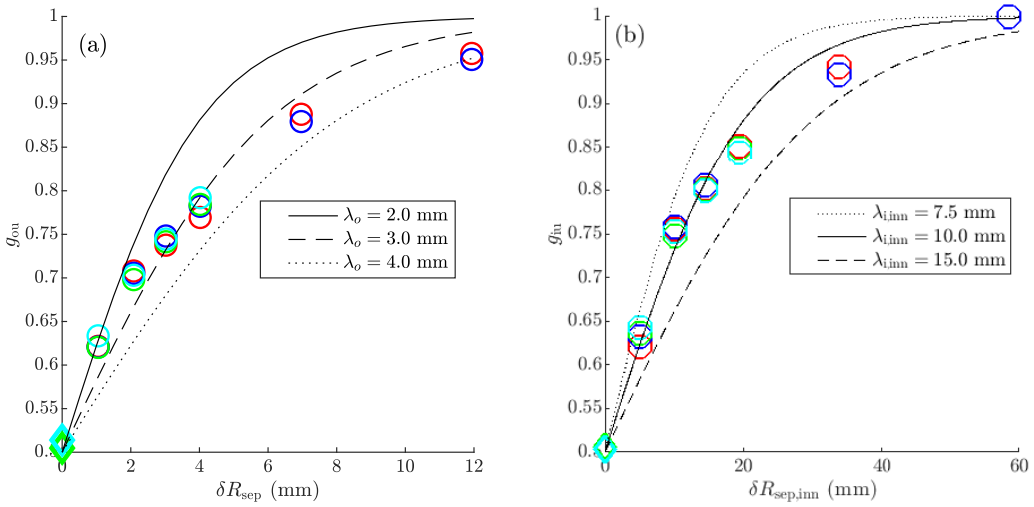

Figure 4: Power fraction to the upper divertor for a) the outboard side, $g_{\rm ou}$ and b) the inboard side, $g_{\rm iu}$. Markers are SOLPS-ITER simulation results whose colors correspond to those in Tab. 2.

Figure 4(a) shows the power fraction to the upper divertor for the outboard side, $g_{\rm ou}$. The dependence of $g_{\rm ou}$ on $\delta R_{\rm sep}$ follows the model for the choice of $\lambda_{\rm o}$ in the model within the range 2 mm $\leq \lambda_{\rm o} \leq$ 4 mm. As for the inboard side in Fig. 4(b), the power fraction to the upper divertor $g_{\rm iu}$ is plotted as a function of the distance of the two separatrices on the inboard side, $\delta R_{\rm sep,inn}$. The simulation results are well-fitted by using $\lambda_{\rm i,inn} \sim 10$ mm.

Now we want to know if those parameters $\lambda_{\rm o}$ and $\lambda_{\rm i,inn}$ are similar to the parallel heat flux decay lengths in the simulation. The parallel heat flux decay lengths $\lambda_{\rm q,out}$ and $\lambda_{\rm q,inn}$ were calculated in the following steps for the outboard side and the inboard side, respectively : i) obtain the total energy flux at the primary divertor entrance, ii) divide the total energy flux by the parallel area at the midplane, iii) map the total energy flux density to the midplane. As shown in Fig. 5, the parallel heat flux decay length on the outboard side appears to be a relatively good estimation ($\lambda_{\rm q,out} \approx \lambda_{\rm o}$) while that on the inboard side shows a significant mismatch between them ($\lambda_{\rm q,inn} \ll \lambda_{\rm i}$).

The observed relationships, $\lambda_{\rm q,out} \approx \lambda_{\rm o}$ and $\lambda_{\rm q,inn} \ll \lambda_{\rm i}$, can be understood from the total energy flux profiles at the divertor entrances. Figure 6 shows the total energy flux density at each divertor entrance for the case No. 4 with $\delta R_{\rm sep}$=2 mm. The parallel

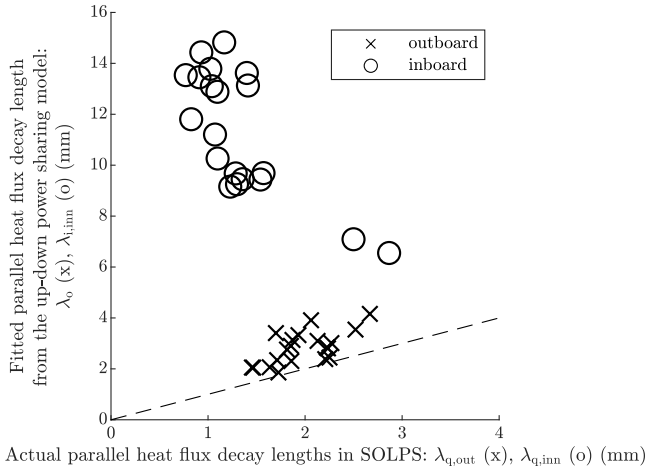

Figure 5: Relationships between the actual parallel heat flux decay lengths $\lambda_{\mathrm{q,out/inn}}$ calculated from the total energy flux density profiles in SOLPS-ITER and the fitted parallel heat flux decay lengths $\lambda_{\mathrm{o/i}}$ obtained by fitting the up-down power sharing to Brunner's model, Eqs. 6 and 7. The dashed line shows $\lambda_{\mathrm{q,out}} = \lambda_{\mathrm{o}}$ (or $\lambda_{\mathrm{q,inn}} = \lambda_{\mathrm{i}}$), which indicates the up-down sharing can be estimated from the parallel heat flux decay length or vice versa.

area at each midplane was chosen to divide the heat flux at the divertor entrances q_{dive} on each side. Positive values of the fluxes are in the direction shown by the arrows in Fig. 6(c).

As shown in Fig. 6(a), the total energy flux density at the upper-outer divertor entrance is well-reproduced by the exponential function and that at the lower-outer divertor entrance is almost on top of it. This picture matches with the assumption of Brunner's model about the energy fluxes towards the upper and the lower divertors, thus we have obtained $\lambda_{\mathrm{q,out}} \approx \lambda_{\mathrm{o}}$ for the outboard side.

This picture does not hold on the inboard side though, as shown in Fig. 6(b). Unlike Fig. 6(a), the energy flux densities at the upper- and the lower-inner divertor entrances do not share a similar profile in the secondary SOL.

There are two reasons for the mismatch between the total energy flux density profiles at A and C in Fig. 6(c) in the secondary SOL. One is the contribution of the convective part of the energy flux. In the inner secondary SOL, there is a convective energy flow upwards, which forms the bump of the total energy flux density at the upper-inner divertor entrance in the secondary SOL and reduces the total energy flux at the lower-inner divertor entrance. The other reason is the additional power source from the outboard side through the primary SOL, crossing the surface "e" in Fig. 6(c). Looking at the values at the primary separatrix, the value at the upper-inner divertor entrance ($\sim$ 1100MW/m^2) is much higher than that at "e" ($\sim$ 200MW/m^2). This indicates that the energy flux at the upper-inner divertor entrance in the primary SOL

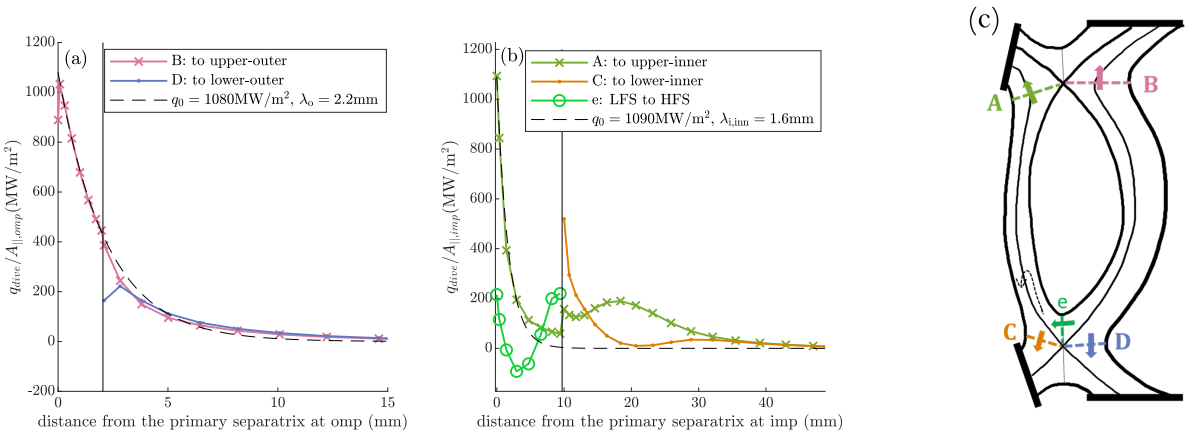

Figure 6: Total energy flux density at the omp, obtained by dividing the total energy flux at each divertor entrance with the parallel area at each midplane: a) the outer divertor entrances and b) the inner divertor entrances. Results shown are for the case No. 4 with δR_{sep}=2 mm.

is dominantly due to the power through the inboard side of the primary separatrix. On the other hand, the energy flux density at the lower-inner divertor entrance in the secondary SOL appears to gain by the power source from the outboard side through the primary SOL, as shown by the dashed black arrow in Fig. 6(c). For the above two reasons, we have obtained $\lambda_{\mathrm{q,inn}} \ll \lambda_{\mathrm{i}}$ - the fraction to the upper divertor is much smaller (i.e. λ_{i} is much larger) than that expected from Brunner's model using the parallel heat flux decay length at the upper-inner divertor entrance $\lambda_{\mathrm{q,inn}}$. It should be noted that the negative value of the energy flux density at "e" is due to the convective flow, which will be addressed in Sec. 4.2.3.2.

4.2 IN-OUT power sharing

As already shown in Fig. 3 (a), the power fraction to the inner divertors did not increase with δR_{sep} in the SOLPS result, whereas it showed a clear increase with increasing δR_{sep} in the experiments[3][7].

Why would the power fraction to the inboard side, "f_{i}", change with δR_{sep}? The change must be explained by 1) the ratio of radial heat transport through the primary separatrix between the HFS and the LFS and/or by 2) a difference in the main SOL losses with δR_{sep} and/or by 3) the in-out power sharing in the primary SOL (between the two separatrices). Each of those points is discussed in this section.

4.2.1 Radial heat flux through the primary separatrix To understand whether any mechanism dominates, we first assess 1) the ratio of radial energy transport through the primary separatrix between HFS and LFS. Figure 7 shows the ratio $P_{\mathrm{sep,HFS}}/P_{\mathrm{sep}}$

obtained in the simulations for $0 \leq \delta R_{\rm sep} \leq 4$mm. It is clearly seen that the ratio is lower in the DDN cases (0 mm $< \delta R_{\rm sep}$) compared to the CDN cases ($\delta R_{\rm sep} = 0$ mm).

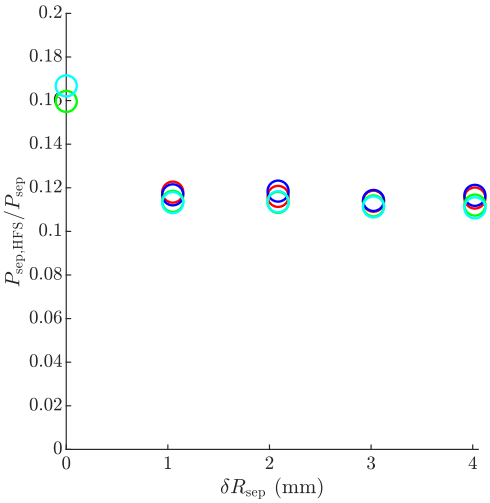

Figure 7: Ratio of the total energy through the primary separatrix on HFS, $P_{\rm sep,HFS}/P_{\rm sep}$.

To understand why it is lower in DDN than in CDN, we first decompose the radial transport into conduction and convection, plotting them along the primary separatrix in the clockwise direction from the bottom, as shown by the coordinate $s_{\rm pol,sep}$ in Fig. 8(a). Figure 8(b) shows the profiles of the radial heat flux density $q_\perp$ for $\delta R_{\rm sep} = 0$ mm and $\delta R_{\rm sep} = 1$ mm of Case No. 4, as representatives of CDN and DDN, respectively. A pronounced difference of the total heat flux density between CDN and DDN is seen in the bottom half of the HFS 0 m $\leq s_{\rm pol,sep} \leq 5$ m, the region circled by the dashed lines and named "X" in Fig. 8(a). By decomposing it into conduction (solid lines) and convection (dotted lines), we find that the difference is dominantly due the conduction, which leads us to focus on the radial conductive heat flux density.

The radial conductive transport is dominated by the anomalous transport. Since we set poloidally constant anomalous radial heat conduction coefficients, $\chi_\perp = \chi_{\rm e\perp} = \chi_{\rm i\perp}$, the radial conductive heat flux density $q_{\perp,\rm cond}$ is given by

$$q_{\perp,\rm cond} = n\chi_\perp \frac{d\left(T_e + T_i\right)}{dy} = n\chi_\perp \frac{dT}{dy}, \tag{13}$$

where n is the plasma density, T_e and T_i are the electron and ion temperature respectively, and y is the radial coordinate. Figures 8(c) and (d) respectively show the decomposed parts of $q_{\perp,\rm cond}$, the temperature gradient dT/dy and the plasma density n. In the region X, 0 m $\leq s_{\rm pol,sep} \leq 5$ m, both of them are larger in CDN than in DDN, contributing to the larger $q_{\perp,\rm cond}$ in the region.

Let us consider the parallel energy flux along the first flux tube surrounding the primary separatrix and resulting temperature profile. In DDN, as shown by the dashed arrow in Fig. 8(a), the "upstream" of the energy flux flowing in the region X $q_{\parallel \rm DDN}$ is

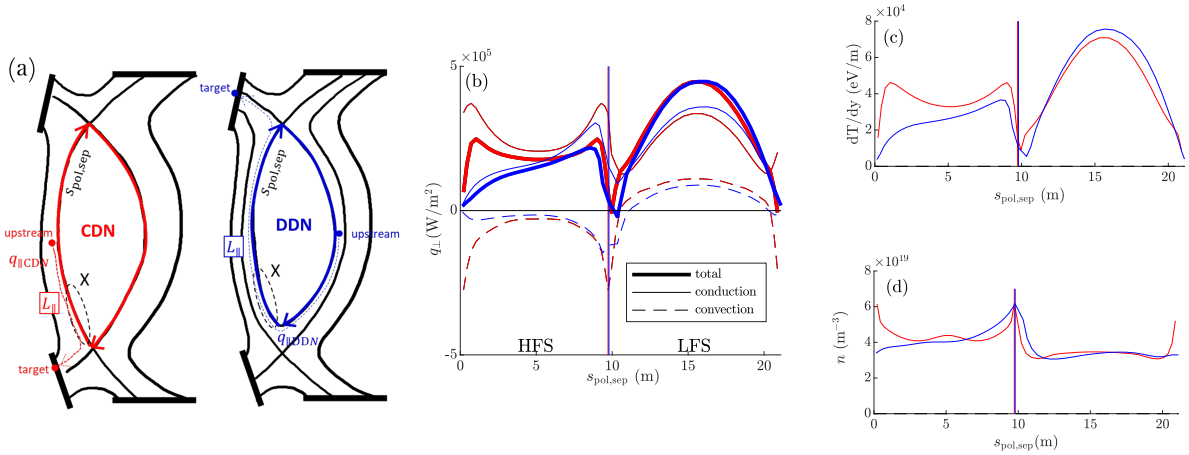

Figure 8: Profiles related to the radial heat flux densities for Case No. 4 along the primary separatrix. The red lines ($\delta R_{\rm sep} = 0$ mm) represent the CDN cases while the blue lines ($\delta R_{\rm sep} = 1$ mm) represent the DDN cases. (a) The coordinate $s_{\rm pol,sep}$ along the primary SOL, (b) the radial heat flux densities: total (thick solid), conduction (solid), convection (dashed), (c) the radial temperature gradient ($T = T_e + T_i$), (d) the plasma density.

located around the outer mid-plane (omp) on the LFS. In CDN, on the other hand, the "upstream" of the energy flux in the region X is around the inner-midplane. This difference leads us to expect $|q_{\parallel \rm DDN}| > |q_{\parallel \rm CDN}|$ as the radial power on the LFS is larger than that on the HFS. In addition, due to the different location of the "upstream", the connection length from the upstream to the corresponding target between DDN and CDN differ. It is approximately a factor 5 larger in DDN in this case. Given the two-point model, $T_{\rm u}^{7/2} \propto L_\parallel q_\parallel$, those two differences make the upstream temperature in CDN lower than that in DDN. Assuming that 1) the temperature in the region X is similar to the temperature at the omp in DDN and 2) the temperature along the LCFS is identical between CDN and DDN, this difference in the upstream temperature makes the radial temperature gradient in the region X higher in CDN compared to DDN. In addition, in the region X of CDN, there is a clear temperature drop towards the bottom X point, which is likely to be caused by an extra radial power loss to the PFR region in the flux tube below the X-point. This makes the significant difference in dT/dy between CDN and DDN in the region X. It appears that the density profiles have peaks near the X-points in Fig. 8(d) in order to reduce the pressure gradient generated by the temperature drops.

Through these ways, the in-out power sharing between CDN and DDN can vary because of the radial transport through the primary SOL. In the investigated cases in this paper, the power fraction to the inboard side f_i was reduced from CDN to DDN mainly because of the reduced radial temperature gradient on the bottom half region of the HFS.

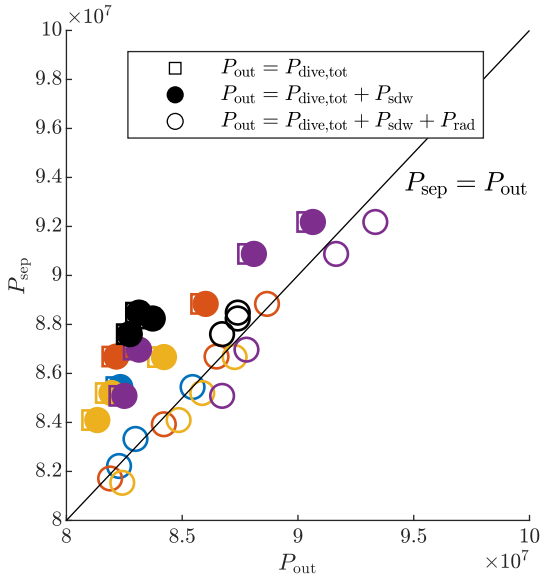

Figure 9: Power coming into the SOL region (=Power crossing the primary separatrix P_{sep}) v.s. power getting out from the SOL region P_{out}. Markers show P_{out} accounting progressively for 3 contributions: the power crossing through the divertor entrances $P_{\mathrm{dive,tot}}$, the power following to the side walls P_{sdw}, and the volumetric power loss by radiation P_{rad}.

4.2.2 Power loss in the main SOL In this section we consider 2) a difference in the main SOL losses with δR_{sep}, by confirming the energy balance in the region from the primary separatrix to the 4 divertor entrances. We consider two power loss mechanisms in the region, the volumetric radiation power loss P_{rad} and the power flowing through the plasma to the side wall (leaving the plasma grid) P_{sdw}. As shown in Fig. 9, the power balance in the region is satisfied with less than 10% contribution of P_{rad} and almost no contribution of P_{sdw}.

Given that neither 1) the radial heat transport nor 2) the main SOL losses explains the behaviour of f_{i} in the DDN cases, we look into the parallel heat transport in the primary SOL in the next section.

4.2.3 The role of parallel heat flux through the primary SOL To discuss in-out power sharing in the primary SOL, we define the power crossing the upper divertor entrances through the primary SOL as $P_{\mathrm{pri,i}}$ and $P_{\mathrm{pri,o}}$ for the inner and outer, respectively, and the in-out power ratio as $K_{\mathrm{i,pri}} \equiv P_{\mathrm{pri,i}}/P_{\mathrm{pri,o}}$ (see Fig. 10(a)). Figure 10(b) shows a summary of this section - the in-out power ratio $K_{\mathrm{i,pri}}$ obtained by SOLPS (colored markers) appears to be lowered by two effects, 1) the total flux compression from outer midplane (omp) to the upper-inner divertor (uid) and 2) the parallel current inducing anti-clockwise heat transport in the primary SOL. Those two effects are discussed in detail in the following subsections.

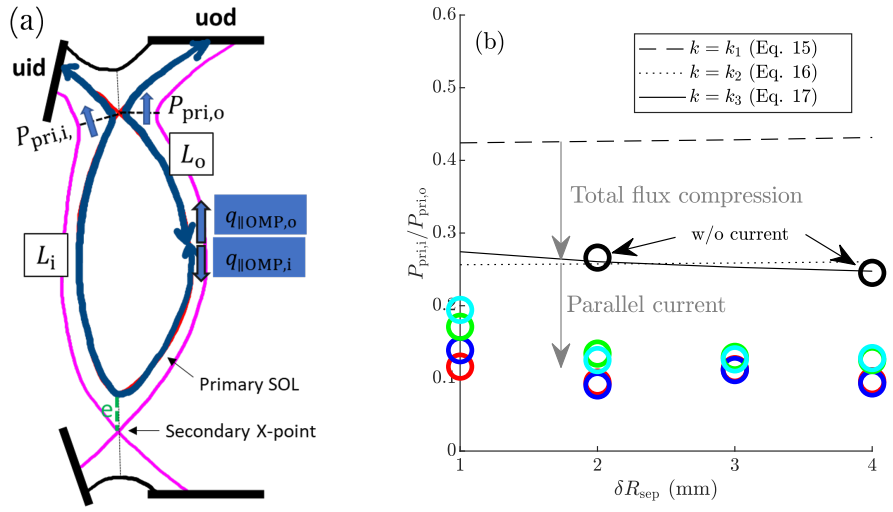

Figure 10: (a) Schematic view of the primary SOL and definition of the in-out power sharing in the primary SOL. (b) In-out power sharing in the primary SOL in SOLPS-ITER simulations (colors as in Tab. 2). The estimations obtained by Eq. 18 for k given by one of Eqs. 15-17; dashed: $k = k_1$ (Eq. 15) i.e. estimation by the connection length ratio, dotted: $k = k_2$ (Eq. 17) i.e. estimation accounting for B-variation with liner approximation, solid: $k = k_3$ (Eq. 16) i.e. estimation accounting for B-variation with full integration.

4.2.3.1 The effect of total flux expansion/compression

In this section we assess the effect of total flux expansion/compression of $|\mathbf{B}|$ along a flux tube on $K_{\mathrm{i,pri}}$. As shown in Fig. 10(a), we assume all of the power through the primary separatrix comes out at the omp and it is separated into $q_{\|\mathrm{OMP_o}}$, the parallel energy flux density flowing to the outer divertor, and $q_{\|\mathrm{OMP_i}}$, that to the inner divertor, on each flux tube. If there is no volumetric power gain/loss and no radial transport in the flux tube, the ratio of the power through the primary inner divertor entrance to that through the primary outer divertor entrance, defined as $k_{\mathrm{i,pri}}$, should be equal to $q_{\|\mathrm{OMP_i}}/q_{\|\mathrm{OMP_o}}$, such that

$$k_{\mathrm{i,pri}} = \frac{q_{\|\mathrm{OMP_i}}}{q_{\|\mathrm{OMP_o}}}. \tag{14}$$

With the additional assumptions that 1) conduction dominates the parallel heat transport, 2) target temperatures are low enough to satisfy $T_t^{7/2} \ll T_u^{7/2}$, and 3) the strength of the total magnetic field $|\mathbf{B}| = B$ is constant along the flux tube, Pitcher & Stangeby's model[14] would lead us to expect

$$\frac{q_{\|\mathrm{OMP_i}}}{q_{\|\mathrm{OMP_o}}} \sim \frac{L_o}{L_i} \equiv k_1, \tag{15}$$

where L_o and L_i are the parallel distances from the omp to the outer and inner divertor targets, respectively (see Fig. 10(a)). The third assumption above, however, is not

well satisfied in STs. Accounting for the B-variation, i.e. flux expansion/compression, changes the ratio as[15]

$$\frac{q_{\parallel \mathrm{OMP_i}}}{q_{\parallel \mathrm{OMP_o}}} \sim \frac{\int_{\mathrm{OMP}}^{uod} \frac{B}{B_{\mathrm{OMP}}} ds}{\int_{\mathrm{uid}}^{OMP} \frac{B}{B_{\mathrm{OMP}}} ds} \equiv k_3. \tag{16}$$

By assuming 1) $|\mathbf{B}|$ is inversely proportional to the radial coordinate R and 2) R is linear with the parallel distance, the ratio can be described with the toroidal flux expansion/compression, $f_{R_o} \equiv B_{\mathrm{OMP}}/B_{\mathrm{ot}} \sim R_{\mathrm{ot}}/R_{\mathrm{OMP}}$ and $f_{R_i} \equiv R_{\mathrm{it}}/R_{\mathrm{OMP}}$, where R_{OMP}, R_{ot}, and R_{it} are respectively the radii at the outer midplane, the upper-outer target, and the upper-inner target of the flux tube, such that

$$\frac{q_{\parallel \mathrm{OMP_i}}}{q_{\parallel \mathrm{OMP_o}}} \sim \frac{L_{\mathrm{o}}}{L_{\mathrm{i}}} \frac{f_{R_{\mathrm{i}}} - 1}{\ln\left(f_{R_{\mathrm{i}}}\right)} \frac{\ln\left(f_{R_{\mathrm{o}}}\right)}{f_{R_{\mathrm{o}}} - 1} \equiv k_2. \tag{17}$$

Since this power ratio (Eqs. 15-17) varies between the individual SOL flux tubes in the primary SOL, a way to average them is required to evaluate the net $K_{\mathrm{i,pri}}$. For this, we weight our estimate for the integrated $K_{\mathrm{i,pri,est}}$ towards those flux tubes which carry more power. We assume the power to be divided at the omp has an exponential-decay form $P\exp(-r_{\mathrm{sep}}/\lambda_q)$, where r_{sep} is the radial distance from the primary separatrix. Using this assumption, the averaged estimation with Eq. 15 for example is

$$K_{\mathrm{i,pri,est}} \equiv \frac{\int_0^{\delta R_{\mathrm{sep}}} P\exp(-r_{\mathrm{sep}}/\lambda_q)\frac{k}{1+k} dr_{\mathrm{sep}}}{\int_0^{\delta R_{\mathrm{sep}}} P\exp(-r_{\mathrm{sep}}/\lambda_q)\frac{1}{1+k} dr_{\mathrm{sep}}}, \quad k = k_1, k_2, k_3. \tag{18}$$

In Fig. 10(b), the lines are the averaged estimations from Eq. 18 with f given by one of Eqs. 15-17. The estimation by the connection length ratio, $L_{\mathrm{o}}/L_{\mathrm{i}}$, is $\sim$0.43, whereas that with $|\mathbf{B}|$-variation is 0.25$\sim$0.28, which means the power fraction to the inner divertor was reduced by the flux expansion/compression. This is a benefit for spherical tokamaks that tend to have strong total flux compression $B/B_{\mathrm{OMP}} > 1$ on the HFS. The approximate form of the magnetic field strength with the factor g_{fR} (Eq. 17) gives us a similar value to the full estimation with the original formula (Eq. 16), with a relative error $<$10%.

4.2.3.2 Contribution of the parallel current

As shown in Fig. 10(b), simulations performed without the parallel current showed an increase of the in-out power ratio in the primary SOL, $K_{\mathrm{i,pri}}$, which implies the parallel current reduced $K_{\mathrm{i,pri}}$ in the originally investigated cases (colored markers in Fig. 10(b)). To understand this effect, we first decompose the total heat flux into the total conduction q_{cond}, the total convection q_{conv}, and the energy flux carried by the electron thermal current q_{thermj}, following Eq.9. Figure 11 shows the decomposed parallel heat flux crossing the upper divertor entrances through the primary SOL. As Fig. 11(a) shows, the total heat flux crossing the inner divertor entrance through the primary SOL is reduced by the convective heat flux that flows in the opposite direction.

This convective heat flux increases the total heat flux at the outer divertor entrance (Fig. 11(b)), though it is a much smaller fraction of the total heat flux compared to that at the inner divertor entrance.

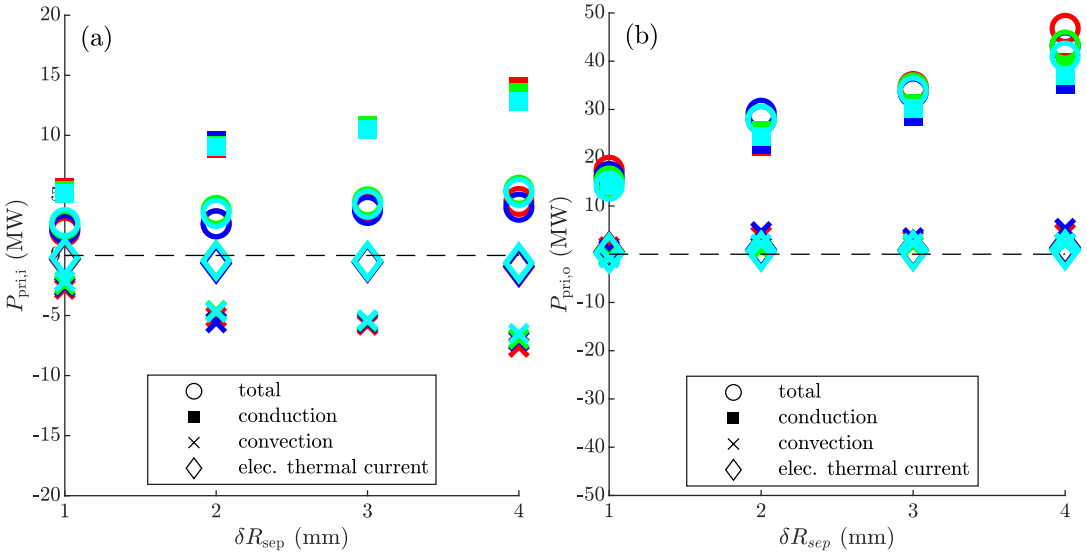

Figure 11: Decomposition of the total heat flux at the divertor entrances of the primary SOL. Positive values: the direction is towards the respective target.

To understand why the convective flux is flowing in the direction that reduces the power to the inner divertor - from the HFS to the LFS - we decomposed the total convective flux into that of electrons and that of ions as introduced in Eq. 11. The terms of Eq. 11 at the upper-inner divertor entrance and at the secondary X-point are shown in Fig. 12 as a function of δR_{sep}. At both locations, the strongest contribution to the convective flow is from the parallel current $j_{\|}$ which flows from LFS to HFS. The strong contribution at the location "e" (marked in Fig. 10(a)) directly tells us that the parallel current in the primary SOL surely reduced $K_{\mathrm{i,pri}}$ in the investigated cases. It should be noted that the electron thermal current q_{thermj} in Eq. 12 has the same contribution as the current-induced convective term in Eq. 11, but the effect is a factor ~ 3.5 smaller due to the prefactor 0.71 instead of the one for the convective term 5/2.

Figure 13(a) shows the parallel current density in the primary SOL at the surface "e" for all the cases. We can confirm that the parallel current flows from the LFS to the HFS in all the cases. There is no clear dependence on δR_{sep}.

In order to understand the physical mechanism of these currents, we integrate Ohm's law for the parallel current density $j_{\|}$ [A/m^2] along a flux tube from the upper-outer divertor target (uod) to the upper-inner divertor target (uid), which gives us

$$j_{\|} = \frac{\bar{\sigma}_{\|} J}{L_{\|}}, J \equiv \left[-(\phi_{\mathrm{uid}} - \phi_{\mathrm{uod}}) + 0.71(T_{\mathrm{e,uid}} - T_{\mathrm{e,uod}}) + \int_{\mathrm{uod}}^{\mathrm{uid}} \frac{1}{n} \frac{dp_{\mathrm{e}}}{ds} ds \right], \qquad (19)$$

where $\bar{\sigma}_{\|}$ [Ω^{-1}m^{-1}] is the parallel electron conductivity, $L_{\|}$ [m] is the connection length from uod to uid, ϕ [eV] is the potential, T_{e} [eV] is the electron temperature, n is the

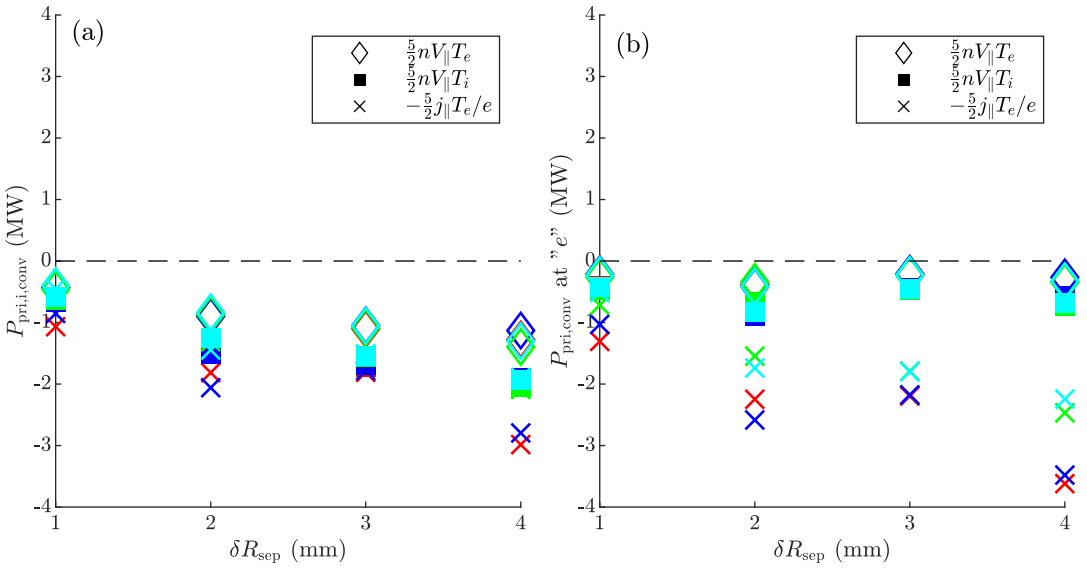

Figure 12: Decomposition of the parallel convective heat flux in the primary SOL a) at the upper-inner divertor entrance and b) at the surface at the secondary X-point, "e" (as shown in Fig. 10(a)).

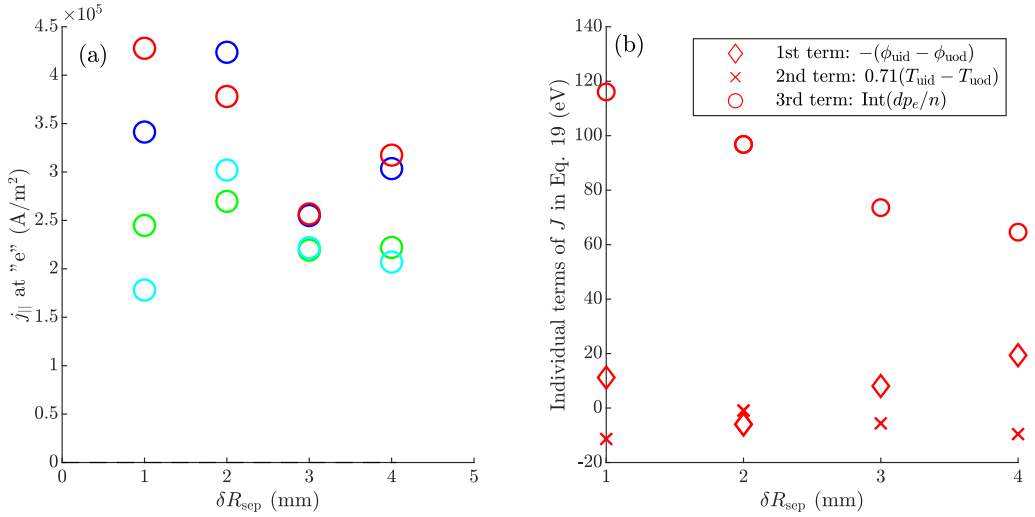

Figure 13: (a) Parallel current density at the surface "e" (shown in Fig. 10(a)) in the primary SOL. (b)Individual terms of J in Eq.19 for the 3rd flux tube in the primary SOL for Case No. 1.

plasma density, p_{e} [eVm^{-3}] is the electron static pressure, and s is the parallel coordinate along the flux tube. J determines the direction of the current - a positive value of J (equally, $j_\parallel$) means that the current flows from the LFS to the HFS. In J, the first term represents the thermal current flowing from a hot target to a cold target. The second term is the thermal force on the ions, which pushes ions in the direction of positive

electron temperature gradient. The third term represents the pressure gradient force pushing electrons faster than the ions, which produces the net current in the opposite direction of the electron flow.

Figure 13(b) shows the individual terms of J in Eq. 19 for Case No. 1 as a function of $\delta R_{\rm sep}$. For simplicity, only those along the 3rd flux tube outward from the primary separatrix in the numerical grid are shown as representative. It is clearly seen that the 3rd term of J, the term with the electron static pressure gradient, is dominant over the other terms. This suggests that the electron pressure gradient and the plasma density play the key roles on the parallel current along the flux tube.

Figure 14 shows the profiles of the plasma density n_e and the electron static pressure p_e along the 3rd flux tube from the upper inner divertor (uid) to the upper outer divertor (uod). If both profiles were symmetric between the two targets, the term $\int_{\rm uod}^{\rm uid} \frac{1}{n}\frac{dp_{\rm e}}{ds}ds$ would be zero. In other words the positive value of the term is induced by the asymmetry of those profiles. Since we integrate from the uod to the uid, the pressure drop towards the uod makes the term larger with positive values of $\frac{dp_{\rm e}}{ds}$, while that towards the uid makes it smaller. The density profile adds a weight to the pressure gradient at each location. In this case, the lower density near the uod weighs more the positive values of $\frac{dp_{\rm e}}{ds}$ there, while the higher density near the uid weighs less the negative values of $\frac{dp_{\rm e}}{ds}$ on the other side. This is how the term $\int_{\rm uod}^{\rm uid} \frac{1}{n}\frac{dp_{\rm e}}{ds}ds$ has got a positive value. In addition to the asymmetry between the two divertor regions, a clear increase of the electron static pressure from the inner midplane (imp) to the upper-inner divertor entrance (uide) in Fig. 14 contributed to the relatively large value of the term $\int_{\rm uod}^{\rm uid} \frac{1}{n}\frac{dp_{\rm e}}{ds}ds$ because the weight from the plasma density is high (i.e. the density is low) in the region. In Sec. 5 it will be discussed how the pressure gradient became positive from the imp to the uide.

As already shown in Fig.10(b), the effect of the parallel current has been confirmed by two simulations with the parallel current artificially zeroed out. As shown by the black points, in the absence of the parallel current, we obtained $\sim 110\%$ increase of the in-out power ratio $P_{\rm pri,i}/P_{\rm pri,o}$ in the primary SOL, which results in $\sim 40\%$ increase of the power fraction to the inner divertors (not shown in this paper).

However, one important question is how universal this contribution of the parallel current would be in the future operational scenarios. Assuming that there should be some pressure gradient near the both targets in the operational scenarios, a key to obtain this parallel current from the uod to the uid is a high density near the uid. This is likely to be the case for a case with high-recycling primary inner divertor, but not for a fully-detached case. It is implied also from Fig. 13 (a) that the parallel current in the primary SOL is smaller in more detached cases - in Fig. 13 (a) the cyan markers are the most detached cases whereas the red markers are the least detached cases as shown in Tab.2. From those results, the parallel current may not be expected in fully-detached scenarios or in attached (i.e. low-recycling) scenarios, but it might appear in a high-recycling regime for the primary inner divertor, leading it to a deeper detachment by transporting convective heat flux from the inner divertor to the outer divertor.

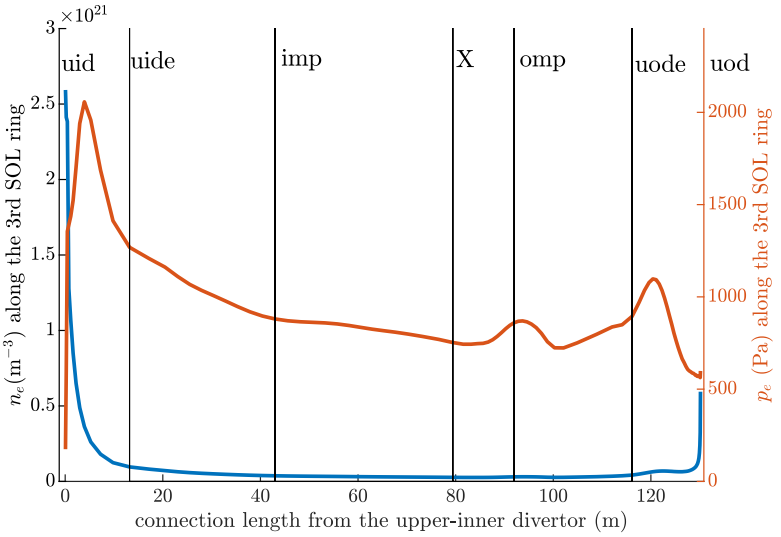

Figure 14: Spacial profiles of the plasma density n_e and the electron static pressure p_e along the 3rd flux tube in the primary SOL from the upper inner divertor (uid) to the upper outer divertor (uod).

5 Discussion

5.1 The electron static pressure along a flux tube in the primary SOL on the HFS

Why is the electron pressure gradient positive from the inner midplane (imp) and the upper-inner divertor entrance (uide) as shown in Fig. 14? This appears to be a result of the net parallel momentum gain in the flux tube due to the radial transport of the parallel momentum, which is caused by the flow reversal in the primary SOL. The blue solid line in Fig. 15(a) shows the total pressure (dynamic pressure of ions + viscosity + ion/electron static pressure) profile along the 3rd flux tube in the primary SOL from as defined as the coordinate s in Fig. 15(b). The total pressure increases from the imp to $s \sim 45$ m, which appears to be gained by the parallel momentum source due to the net radial flux of convection and viscosity $S_{\mathrm{m}\parallel\mathrm{RT}}$, shown by the blue dashed line. The net radial momentum flux depends on the radial gradient of the parallel velocity, thus the second radial derivative of the parallel velocity, plotted with the orange line, shows a good correlation with $S_{\mathrm{m}\parallel\mathrm{RT}}$. The interpretation of this momentum source is given in Fig. 15(b). In the investigated cases, due to the strong recycling source at the upper inner divertor, the plasma flow is reversed in the primary SOL in the region from uid to imp. With $V_\parallel < 0$, a positive value of $d^2V_\parallel/(dr^2)$ at the 3rd flux tube means that the negative momentum source from the 2nd flux tube is smaller than the negative momentum loss to the 4th flux tube, under the assumption that the radial transport is constant and pointing outwards. As shown in Fig. 15(b), this brings a net radial loss of negative parallel momentum, i.e. a gain of positive parallel momentum. Although it is not necessarily the electron static pressure that is gained by the momentum source, this mechanism in the flow reversal condition appears to be a possible explanation for the positive electron pressure gradient towards the upper inner divertor and resulting parallel current flowing from the LFS to the HFS in the primary SOL.

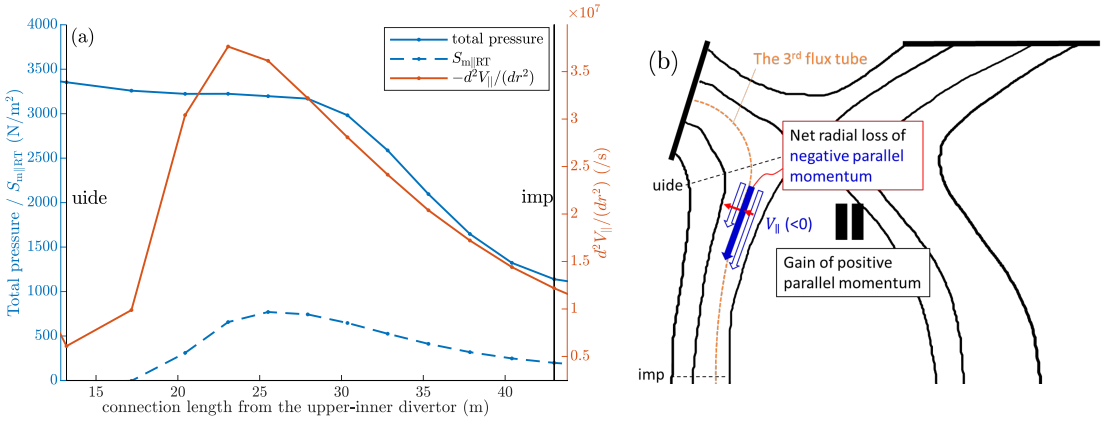

Figure 15: (a) Spatial profiles of the total pressure (dynamic pressure of ions + viscosity + ion/electron static pressure), the parallel momentum source due to the net radial flux of convection and viscosity $S_{\mathrm{m}\|\mathrm{RT}}$, and the second derivative of the parallel velocity $d^2V_{\|}/dr^2$ along the third flux tube in the primary SOL from the uide to the imp. (b) Schematic view of the relationship between the momentum source $S_{\mathrm{m}\|\mathrm{RT}}$ and $d^2V_{\|}/dr^2$.

6 Conclusion

The impact of disconnection of the two separatrices on the power-sharing between the 4 divertors in a disconnected-double-null configuration was investigated on an early STEP design. Overall, SOLPS-ITER simulation results (without drifts) showed less significant impact on the power fraction to the inner divertors as a funtion of $\delta R_{\mathrm{sep}}/\lambda_q$ compared to the experimental results on current machines. At the highest δR_{sep} the total power fraction to the inner divertors was $\sim 20\%$, which is similar to the experimental result on MAST[3] and is lower than those on conventional tokamaks. This indicates the benefit of a double-null configuration may be less on STEP than what we expected from the previous experiments on conventional tokamaks, in terms of the power loading onto inner divertor targets.

To understand the overall power-sharing, the up-down sharing and in-out sharing were separately investigated. Findings from the up-down sharing are:

- up-down sharing (outer): profiles of the parallel heat flux density at the divertor entrances agree well to what Brunner's model expects. Thus the parallel heat flux decay length obtained in the SOLPS-ITER agrees well to the fitted parallel heat flux decay length from the up-down power sharing model, which indicates that the actual parallel heat flux decay length on the outboard side is a good indicator of the up-down power sharing, or vice versa.
- up-down sharing (inner): profiles of the parallel heat flux density at the divertor entrances did not agree well to Brunner's model. This is because of the combined effects - the power radially crossing the HFS primary separatrix and the power coming from the LFS by the parallel transport in the primary SOL. For this reason we obtained much smaller actual parallel heat flux decay length in the simulation than the fitted parallel heat flux decay length from the up-down power sharing model. Further study is required to understand the relationship between them.

The in-out power sharing was discussed separately by 1) the ratio of radial heat transport through the primary separatrix between the HFS and the LFS, 2) power loss in the main SOL, and 3) the in-out power sharing in the primary SOL (between the two separatrices)

- in-out sharing 1) the radial flux through the primary separatrix: The power fraction to the inboard side was $\sim 12\%$ in DDN and $\sim 16\%$ in CDN. This difference is due to the reduced amount of the conductive (anomalous) part of the radial heat flux along the primary separatrix in the bottom half region on the HFS in DDN, which was mainly due to the smaller radial temperature gradient in that region in DDN compared to CDN. This was caused by two features of the temperature profiles in the first flux tube outward from the primary separatrix on the HFS bottom half region: 1) higher temperature in DDN than in CDN due to the contribution from the parallel heat flux from the LFS and 2) temperature drop from the inner midplane to the bottom X-point. Since it is a fundamental difference between CDN and DDN, we presume this difference of the in-out power ratio would appear

in future simulations when the same profiles of the radial transport coefficients were set for CDN and DDN. However it is remained an open question what would happen in experiments.

- in-out sharing 2) The two power loss mechanism considered - the radiation loss and the power through the plasma to the side walls - had less than 10% contribution in total to the entire power balance.
- in-out sharing 3) the parallel flux through the primary SOL: Using Stangeby & Pitcher's model, we have shown that the flux expansion/compression from the outer-midplane to each divertor target in the STEP design would reduce the power fraction to the inner divertor, which is an operationally useful feature of spherical tokamaks (STs). A further decrease of the power fraction to the inner divertor was obtained by the convective heat flow from the LFS to the HFS induced by the parallel current in the primary SOL. The parallel current is caused by the positive pressure gradient towards the upper-inner target which is occurring together with the plasma reversed flow in the upper-inner divertor region.
  Simulations without parallel current showed a good agreement with Stangeby & Pitcher's model with flux expansion/compression effect. This convinced us that there is the effect of flux expansion/compression on the in-out power sharing in the primary SOL as estimated by the model, and additionally there is a reduction of the ratio to the inner by the parallel current. While the latter appears to be case-dependant, we presume the former should be universal for STs.

For better understanding of the power-sharing in DDN, comparative study between Brunner's model, SOLPS-ITER simulation, and experiments is ongoing on MAST, including the drift terms. Use of more advanced versions of SOLPS-ITER code is also important on this subject. Another studies addressing the effects of the assumed radial transport coefficients and drifts are ongoing on STEP.

Acknowledgements

This work has been funded by STEP, a UKAEA program to design and build a prototype fusion energy plant and a path to commercial fusion.

References

[1] B. J. Braams et al., in Plasma Physics and Controlled Nuclear Fusion Reserach 1984, Vol. 2, IAEA, Vienna (1985) 125.
[2] R. Marchand et al., Nuclear Fusion 35 No. 3 (1995) 297-304.
[3] G. D. Temmerman et al., Plasma Phys. Control. Fusion 52 (2010) 095005 (14pp) doi:10.1088/0741-3335/52/9/095005.
[4] A. Kirk et al., J. Nucl. Mater. 313-316 (2003) 1081-1084.
[5] G. D. Temmerman et al., J. Nucl. Mater. 415 (2011) S383-S386.
[6] T. W. Petrie et al., J. Nucl. Mater. 290 (2001) 935-9.
[7] D. Brunner et al., Nucl. Fusion 58 (2018) 076010 https://doi.org/10.1088/1741-4326/aac006.

[8] Private Communication.
[9] T. W. Petrie et al., A Comparison of Plasma Performance Between Single-Null and Double-Null Configurations During Elming H-Mode (1999). https://www.osti.gov/servlets/purl/766942
[10] Dekeyser et al., Plasma and Fusion Res. (2016) https://doi.org/10.1585/pfr.11.1403103
[11] S. Wiesen et al., J. Nucl. Mater. 463 (2015) 480-484.
[12] X. Bonnin et al., Plasma Fusion Res. 11 (2016) 1403102.
[13] R. Pitts et al., Nuclear Materials and Energy 20 (2019) 100696.
[14] C. S. Pitcher and P. C. Stangeby, Plasma Phys. Control. Fusion 39 (1997) 779.
[15] T. W. Petrie et al.,Nucl. Fusion 53 (2013) 113024.